Supplementary Information

"Spin liquid and ferroelectricity close to a quantum critical point in PbCuTe$_2$O$_6$"

Christian Thurn[1*], Paul Eibisch[1], Arif Ata[1], Maximilian Winkler[2], Peter Lunkenheimer[2],

István Kézsmárki[2], Ulrich Tutsch[1], Yohei Saito[1], Steffi Hartmann[1], Jan Zimmermann[1],

Abanoub R. N. Hanna[3,4], A. T. M. Nazmul Islam[4], Shravani Chillal[4], Bella Lake[3,4],

Bernd Wolf[1], Michael Lang[1]

[1]Physikalisches Institut, J.W. Goethe-Universität Frankfurt(M), 60438 Frankfurt, Max-von-Laue-Str.1, Germany

[2]Experimentalphysik V, Zentrum für Elektronische Korrelationen und Magnetismus, Universität Augsburg, Universitätsstr. 1, 86159 Augsburg, Germany

[3]Institut für Festkörperforschung, Technische Universität Berlin, Hardenbergstr. 36, 10623 Berlin, Germany

[4]Helmholtz-Zentrum Berlin für Materialien und Energie, Hahn-Meitner Platz 1, 14109 Berlin, Germany

*e-mail: Thurn@Physik.uni-frankfurt.de

Supplementary Notes

1. Crystal structure, structural motives and magnetic as well as dielectric units of PbCuTe$_2$O$_6$

PbCuTe$_2$O$_6$ crystallizes in a non-centrosymmetric cubic structure with space group P4$_1$32 (No. 213), see Fig. 1. According to density functional theory calculations [1] based on room-temperature structural data, the magnetic lattice can be described by isolated equilateral $S = 1/2$ triangles with nearest-neighbour interaction $J_1 = 1.13$ meV, which are coupled via the second-nearest neighbour interaction $J_2 = 1.07$ meV into a hyperkagome lattice (Fig. 1b). The weaker third- and fourth-nearest neighbour interactions $J_3 = 0.59$ meV and $J_4 = 0.12$ meV couple the spins into chains. Another unique feature of PbCuTe$_2$O$_6$, which has been largely ignored until now, relates to its dielectric degrees of freedom [2]. The material contains polar building blocks originating from the free electron pairs (lone pairs) of the Te^{4+} ions in the oxotellurate tetrahedrons and the asymmetrically coordinated Pb^{2+} ions. These characteristics together with the non-centrosymmetric structure imply the possibility of ferroelectric order interacting with the strongly frustrated quantum spin system.

2. Specific heat and magnetic Grüneisen parameter

At low temperatures ($T < 1.6$ K) there are basically two different contributions to the specific heat, C, of PbCuTe$_2$O$_6$. The first one, C_e, arises from the magnetic moments associated with the spins $\vec{S}$ of the 3d electrons of the Cu^{2+} ions, and the second one, C_n, is due to the magnetic moments of the ^{207}Pb, ^{125}Te, ^{63}Cu and ^{65}Cu nuclei. The phonon contribution C_{ph} [3], however, is negligibly small and does not exceed 1 % of C_e for $T < 1.6$ K. Below $T \approx 0.1$ K the nuclear contribution dominates and has to be determined quite accurately in order to extract C_e reliably from the measured total specific heat C.

The contributions $C_{n,i}$ of the above listed nuclei to the specific heat are Schottky anomalies with equidistant energy levels produced by the different orientations of the nuclear magnetic moments $\vec{\mu}_i$ in the local magnetic fields $\vec{B}_i^*$:

$$C_{n,i} \;=\; z_i \cdot \frac{R}{2} \cdot \left(\frac{\Delta_i}{k_B T}\right)^2 \cdot \left(\frac{1}{\cosh\!\left(\frac{\Delta_i}{k_B T}\right)-1} - \frac{a_i^2}{\cosh\!\left(\frac{a_i \Delta_i}{k_B T}\right)-1}\right) \cdot \qquad (1)$$

Here z_i denotes the number of nuclei of type i in one formula unit, $a_i = 2 \cdot I_i + 1$ (with I_i the nuclear spin quantum number) is the number of energy levels of such a nucleus in the local magnetic field $\vec{B}_i^*$ and $\Delta_i = \mu_i \cdot B_i^*/I_i$ (where $B_i^* = |\vec{B}_i^*|$, $\mu_i = |\vec{\mu}_i|$) describes the spacing between neighbouring energy levels of a nucleus of type i. In the case of the ^{207}Pb and ^{125}Te nuclei $\vec{B}_i^*$ is identical to the external magnetic field $\vec{B}$, as there are no electronic magnetic moments in the vicinity which would produce a (significant) disturbance of the magnetic field. Thus $C_{n,i}$ can be calculated easily by using the corresponding parameters from the table 1 below [4,5]. For the copper nuclei, however, $\vec{B}_i^*$ is strongly influenced by the magnetic field $\vec{B}_e$ from the magnetic moment of the 3d electrons of the Cu^{2+} ion. Therefore, $B_e = |\vec{B}_e|$ has to be determined by asymptotically fitting the low temperature specific heat C in $|\vec{B}| = B = 0$ with the formula (1) using the corresponding parameters of the copper nuclei and leaving $B^*_{Cu63} = B^*_{Cu65} = B_e$ as free parameter (the other nuclei do not contribute in this case, as they do not experience a local magnetic field. The fit is shown in the inset of Fig. 2 and yields the value $B_e = 10.2$ T.

The magnetic Grüneisen parameter $\Gamma_{B,e}$ of the electron spins can be extracted from the measured magnetic Grüneisen parameter $\Gamma_B = T^{-1}\cdot(\partial T/\partial B)_S$ of the total system by taking the specific heat contributions C_i and magnetic Grüneisen parameters $\Gamma_{B,i}$ of all relevant subsystems into account. In general, the following relation holds:

$$\Gamma_B \;=\; \frac{1}{C} \cdot \sum_i C_i \cdot \Gamma_{B,i} \qquad (2)$$

with $C = \sum_i C_i$ the total specific heat. In the case of PbCuTe$_2$O$_6$, $\Gamma_{B,e}$ is then given by

$$\Gamma_B = \frac{1}{C} \cdot (C_e \cdot \Gamma_{B,e} + C_{nPb} \cdot \Gamma_{B,nPb} + C_{nTe} \cdot \Gamma_{B,nTe} + C_{nCu} \cdot \Gamma_{B,nCu}) . \qquad (3)$$

The nuclear magnetic moments of tellurium and lead behave as Langevin paramagnets (for which the entropy $S = S(T/B)$) with the local magnetic field $\vec{B}_i^*$ being identical to the external magnetic field $\vec{B}$, so that

$$\Gamma_{B,nPb} = \Gamma_{B,nTe} = \frac{1}{B} . \qquad (4)$$

For $\Gamma_{B,nCu}$ the situation is less simple due to the strong influence of $\vec{B}_e$ on $\vec{B}_i^*$. As the magnetic moments of the copper nuclei practically do not interact with one another, their T/B_i^* ratio is constant in an adiabatic process:

$$\frac{T}{B_i^*} = const. \qquad (5)$$

The local field is given by

$$B_i^* = \sqrt{B_e^2 + B^2 + 2B_e B \cos\vartheta} , \qquad (6)$$

with ϑ being the angle between $\vec{B}$ and $\vec{B}_e$. Thus the following expression is obtained

$$\Gamma_{B,Cu} = \frac{1}{T} \cdot \left(\frac{\partial T}{\partial B}\right)_S = \frac{B + B_e \cos\vartheta}{B_e^2 + B^2 + 2B_e B \cos\vartheta} . \qquad (7)$$

This can be simplified for the case $B \ll B_e$ by a series expansion and taking into account only the terms which are linear in B/B_e:

$$\Gamma_{B,nCu} = \frac{1}{B_e} \cdot \left[\cos\vartheta + (1 - 2\cos^2\vartheta) \cdot \frac{B}{B_e}\right] . \qquad (8)$$

As the copper spins show no indications of ordering in a small external magnetic field $\vec{B}$, they can be assumed to be oriented completely randomly relatively to $\vec{B}$ and thus the same holds for $\vec{B}_e$ too. Therefore, (8) has to be averaged evenly over the whole solid angle:

$$\overline{\Gamma}_{B,\mathrm{nCu}} = \frac{1}{4\pi} \cdot \int \Gamma_{B,\mathrm{nCu}} d\Omega = \frac{B}{3B_{\mathrm{e}}^2} \quad . \tag{9}$$

Substituting (4, 9) into (3) and solving the equation for $\Gamma_{B,\mathrm{e}}$ yields the final formula

$$\Gamma_{B,\mathrm{e}} = \frac{1}{C_{\mathrm{e}}} \cdot \left[C \cdot \Gamma_B - (C_{\mathrm{nPb}} + C_{\mathrm{nTe}}) \cdot \frac{1}{B} - C_{\mathrm{nCu}} \cdot \frac{B}{3B_{\mathrm{e}}^2} \right] \quad . \tag{10}$$

Figure 2 shows the specific heat contribution, C_{e}, associated with the Cu^{2+} electron spins of $PbCuTe_2O_6$ for two single crystals sc #1(b) and #5(b). The specific heat for both crystals is almost identical around the phase transition anomaly and for temperatures below. Some differences are visible for temperatures above the phase transition where $C(T)$ for #1(b) is slightly higher than $C(T)$ for #5(b).

(1) The first technique applied [6] follows the definition $\Gamma_B = T^{-1}(\partial T/\partial B)_S$, by measuring temperature changes ΔT^* of the sample, which is in weak thermal contact to a bath at temperature T_{b}, in response to changes of the magnetic field ΔB, i.e., $\Gamma_B \approx T^{-1} \cdot (\Delta T^*/\Delta B)_{S \approx \mathrm{const.}}$. A typical measuring cycle is shown in Fig. 3. Since this technique measures the total Grüneisen parameter Γ_B, which is the sum of various contributions (see eq. (3)), the determination of the electronic part $\Gamma_{B,\mathrm{e}}$ requires a careful consideration of the nuclear contributions according to eq. (10).

2) As an alternative approach, we took advantage of the identity $\Gamma_{B,\mathrm{e}} = -C_{\mathrm{e}}^{-1} \cdot (\partial M/\partial T)$ by using the electronic specific heat data, C_{e}, of sc #5(b) shown in Fig. 1 of the main text, and the magnetization, $M(T)$, of sc #5(b) displayed in the inset of Fig. 5 of the main text. The so-derived $\Gamma_{B,\mathrm{e}}$ is also shown in Fig. 4 (blue spheres). As the figure demonstrates, we find a good agreement between the results obtained by following these different approaches. In particular, both approaches reveal a divergence of $\Gamma_{B,\mathrm{e}}(T)$ for $T \to 0$.

3. Thermal expansion

Figure 6 shows the coefficient of thermal expansion of $PbCuTe_2O_6$ single crystals sc #1(a) along the [1-10] and #sc 5(c) along the [110] direction for $T \leq 2$ K.

In the dilatometer cell used (constructed following the design discussed in [7]), the spring leafs, suspending the movable part, exert a force **F** to the sample along the measuring direction, with $F \approx 0.03$ N – 3 N, the actual strength of which depends on the chosen starting capacitance C_s. This results in a uniaxial pressure along the measuring direction $p_{ua} = F/A$ with A the cross-sectional area of the sample, typically ranging from $p_{ua} \approx 0.01$ MPa – 5 MPa.

The data in Fig. 6 represent two data sets taken along an in-plane diagonal: the data for sc #1(a) (green squares) were taken with a uniaxial pressure of moderate strength $p_{ua} = (2.3 \pm 0.5)$ MPa, whereas for sc #5(c) (blue squares) the uniaxial pressure was relatively high with $p_{ua} = (6.5 \pm 1.3)$ MPa. The pressure values refer to values at low temperatures around 4 K. The data sets show practically identical behaviour at the high-temperature end, i.e., from around 2 K down to about 1.4 K. For lower temperatures, both data sets show anomalous behaviour, which is qualitatively similar, albeit with different amplitudes. We assign these differences to the influence of the uniaxial pressure on the domain structure associated with the formation of ferroelectric order around 1 K and the accompanying lattice distortions to a non-cubic low-temperature state. The data for sc #5(c) demonstrate that for a preferential domain orientation – or even a mono-domain configuration – realized here, the anomaly in the coefficient of thermal expansion accompanying the ferroelectric order becomes more pronounced.

4. Magnetic susceptibility

The main panel of figure 7 exhibits the ac-susceptibility of crystal #5(b) as a function of temperature for 0.1 K $\leq T \leq$ 1.6 K in a magnetic field of 0.1 T. The data were taken by using a home-made ac-susceptometer adapted to a top-loading dilution refrigerator. The ac-susceptometer was calibrated via magnetization measurements up to 5 T by comparing the results with data obtained by using a SQUID magnetometer (Quantum Design MPMS). For the χ_{ac} measurements the external field was aligned along the [100] (red filled circles, right scale) and [110] (blue filled circles, left scale) directions. Unlike specific heat, thermal expansion and dielectric experiments, all of which showing pronounced phase transition anomalies around 1 K, no indications for a phase transition are visible in the magnetic response. The g-factor anisotropy for the two field orientations amounts to approximately 5 %, an anisotropy which is typical for Cu^{2+} in a square-planar environment [8]. In the inset the results from the ac-susceptibility measurements for $T \leq$ 1.6 K are shown together with the static susceptibility data of sc # 5(b) (red and blue squares) taken by using a commercial Quantum Design SQUID magnetometer in the temperature range 2.0 K $\leq T \leq$ 20.0 K for the same field orientations. The data reveal a small anomaly around 6 K of unknown origin. A more pronounced anomaly is also visible in the same temperature range for sc #2 (not shown). In this sample sc #2 there is also a small but distinct difference visible between field-cooled and zero-field cooled data. Similar anomalies in this temperature range were also observed in other frustrated triangular-lattice systems and were ascribed to a spin freezing induced by quenched disorder [9].

5. Elastic constant

Figure 8 exhibits the thermal expansion $\alpha_{[110]}$ (orange circles, sc #2) and the longitudinal elastic constant $c_{L[110]}$ (blue squares, sc #5(a)) both as a function of temperature for 1.3 K $\leq T \leq$ 20.0 K. The elastic constant was also measured along the [110] direction. The thermal expansion of sample sc #2 continuously decreases and exhibits a small hump-like anomaly around 7 K. With further decreasing temperature

there is a significant increase of $\alpha_{[110]}$ below 2.2 K which is the precursor of the ferroelectric transition at the $T_{FE} \approx 1$ K, cf. Fig. 2 in the main text. For the longitudinal elastic constant along the [110] direction, we observe a continuous increase of $c_{L[110]}$ upon cooling from room temperature down to approximately 10 K where it adopts a broad maximum. Below 10 K c_L decreases moderately strongly down to 1.3 K, the lowest temperature of our experiment. Below approximately 2 K the softening becomes stronger which we interpret - in analogy to the thermal expansion - as a precursor of the ferroelectric transition.

6. Dielectric constant

The dielectric constant ε' was measured on 3 single crystals of $PbCuTe_2O_6$ in the temperature range 0.25 K $\leq T \leq$ 1.3 K, see Figure 9. In these measurements the electrical field **E** was oriented parallel to the [110] direction for sc #5(b) and sc #1(a), and parallel to the [001] direction for sc #4. For the determination of the dielectric constant ε', a plate capacitor geometry was realized by attaching two electrodes (silver paste) to opposite parallel surfaces of the samples. The dielectric constant was then derived from the capacitance, read out by using an LCR meter (Agilent E4980), and the geometrical dimensions of the plate capacitor. This procedure implies an uncertainty of about $\pm$ 5 %. For all single crystals investigated, we observe a peak in ε' with small variations in the peak position at (0.97 $\pm$ 0.05) K. There is, however, some variation in the size of the peaks, even for the same orientation of the electrical field, indicating some sample-to-sample dependence. The relatively narrow peak sits on top of a temperature-independent background contribution ε_b'. We find similarly high values around $\varepsilon_b' \approx 18$ for sc #5(b) and sc #1(a) for **E** parallel [110] and an even higher value of $\varepsilon_b' \approx 23$ for sc #4 where **E** was parallel to [001]. In contrast, for the pressed-powder sample pd #I(b), we find a reduced $\varepsilon_b' \approx 12$ and only a tiny anomaly around 1 K. From the size of the anomaly and the fact that thermal expansion measurements failed to detect any lattice distortion associated with it (see Fig. 2 main text), we claim

that there is no bulk ferroelectric transition in the investigated pressed-powder samples.

7. Grain-size effect of ferroelectric order

The observation made here of a ferroelectric transition in $PbCuTe_2O_6$ single crystals and the suppression of this transition in pressed-powder samples is consistent with results on grain-size effects in ferroelectric ceramics [10-12], yielding a critical grain size below which the transition disappears. Whereas for an isolated grain the instability of the ferroelectric phase is mainly due to the surface effect, the situation becomes more complex for ceramics where beside intrinsic grain-size effects other factors, which may change with the size of the system, can be of relevance as well, see ref. [12] and references cited therein.

8. Pyrocurrent

Figure 10a provides examples of the pyrocurrent results used to deduce the temperature-dependent electric polarization curves shown in Fig. 4 as described in the methods section of the main text. Typical results for two different positive prepoling fields with a standard heating rate of 60 mK/min, used for all measurements in Fig. 4, are shown. The peak revealed at the transition temperature reflects the successive reorientation of the poled electrical dipoles into disordered equilibrium positions upon heating. As expected, the pyrocurrent is enhanced for higher poling field, corresponding to stronger polarization.

Figure 10b shows the pyrocurrent for two different heating rates and identical, negative prepoling fields. As expected, the current is enhanced for higher rate. For conducting materials, thermally stimulated discharge currents can also lead to pyrocurrent peaks.

The fact that the peak temperature in Fig. 10b is unaffected by the heating rate excludes this non-intrinsic effect, which should lead to a significant shift of the peak to higher temperatures for higher heating rates [13,14].

Supplementary Figures
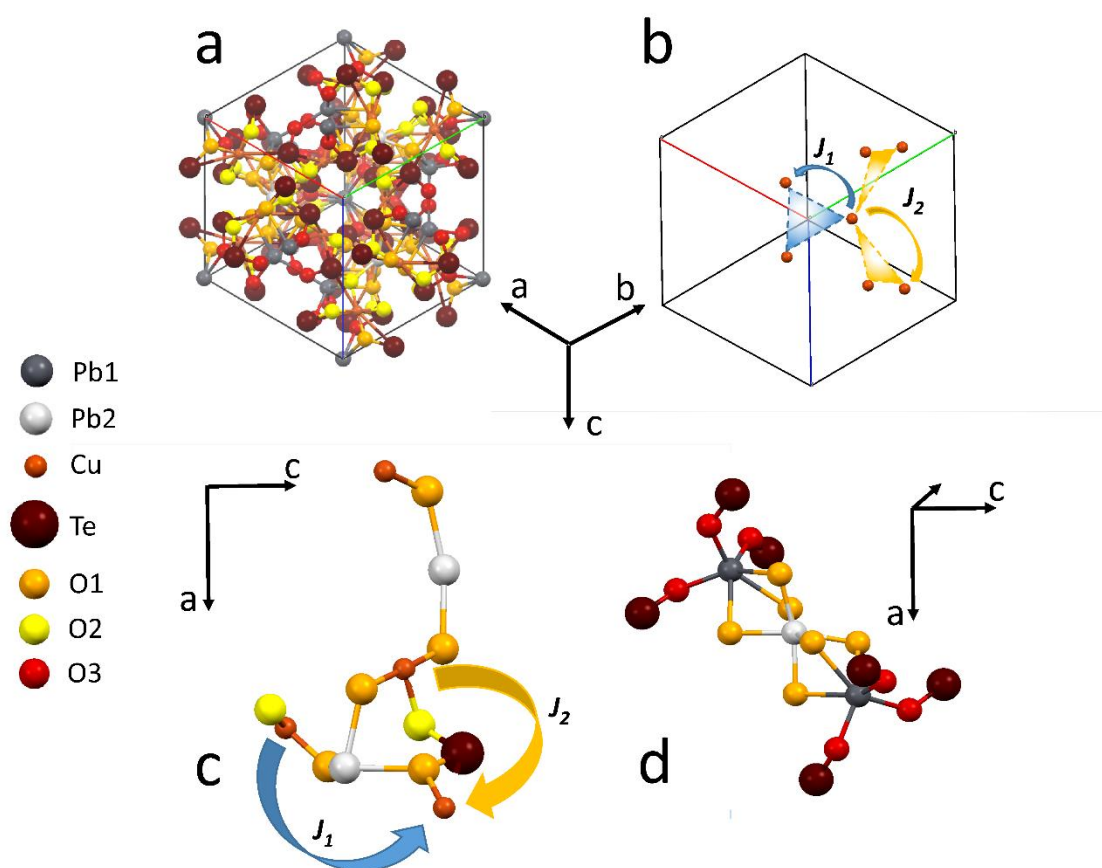
Figure 1. Crystal structure, structural motives and functional units of $PbCuTe_2O_6$. For the atoms in all subfigures a colour code is used as indicated in the figure: Pb1 dark grey, Pb2 light grey, Cu dark orange, Te brown, O1 dark yellow, O2 yellow and O3 red.

a: View along the [111]-direction of the cubic high-temperature structure with space group $P4_132$. The figure shows one unit cell containing 12 crystallographically equivalent magnetic Cu^{2+} ions with $S = 1/2$ forming a three-dimensional (3D) geometrically frustrated hyperkagome lattice.

b: Reduced magnetic structure containing the key motifs. These are equilateral triangles formed by the Cu^{2+} ($S = 1/2$) ions representing the two dominant 1st (blue) and 2nd (yellow) nearest-neighbour interactions with corresponding magnetic coupling constants J_1 and J_2 [1]. Whereas the blue triangles form isolated magnetic units, the yellow ones build a 3D hyperkagome network (not shown here; see, e.g., Fig. 1 of ref. 1) of corner-sharing triangles.

c: Magnetic exchange paths corresponding to J_1 and J_2 for the isolated triangles (blue arrow) and the 3D network of corner-sharing triangles (yellow arrow), respectively. Whereas J_1 (blue arrow) is mediated via the Cu-O1-Pb2-O1-Cu orbital overlap, J_2 (yellow arrow) results from the Cu-O2-Te-O1-Cu orbital overlap.

d: The dielectric unit consists of chiral tellurate complexes and the $Pb1^{2+}$ and $Pb2^{2+}$ ions possessing stereochemically active lone pairs of their 6s electrons. These dielectric units form chains along the [111]-direction, a three-fold rotation axis of the cubic high-temperature structure. The Pb1 ions are in a distorted oxygen coordination with three short bonds to the O3 ions and three long bonds to O1 ions. These long bonds provide a void for the lone pair electrons of Pb1. In contrast, there is no lone pair associated with Pb2 in its symmetrically coordinated environment, forming bonds of similar length to six O1 ions. Therefore, in the non-distorted high-temperature structure the dipole moments originating from the tellurates and Pb1 within each unit compensate each other. Thus a distortion along the three-fold rotation axis, i.e., a displacement of the Pb2 out of its high-symmetry position, is necessary to allow for a (sp) hybridization [15] resulting in the formation of a lone pair with asymmetric electron distribution prerequisite to the formation of ferroelectric order. This process can be described as a second-order Jahn-Teller instability [15]. As the O1 p orbitals are involved in the dominant magnetic exchange paths, we expect that the distorted structure (with the modified electron distribution) will also result in a change in the magnetic coupling constants J_1 and J_2.
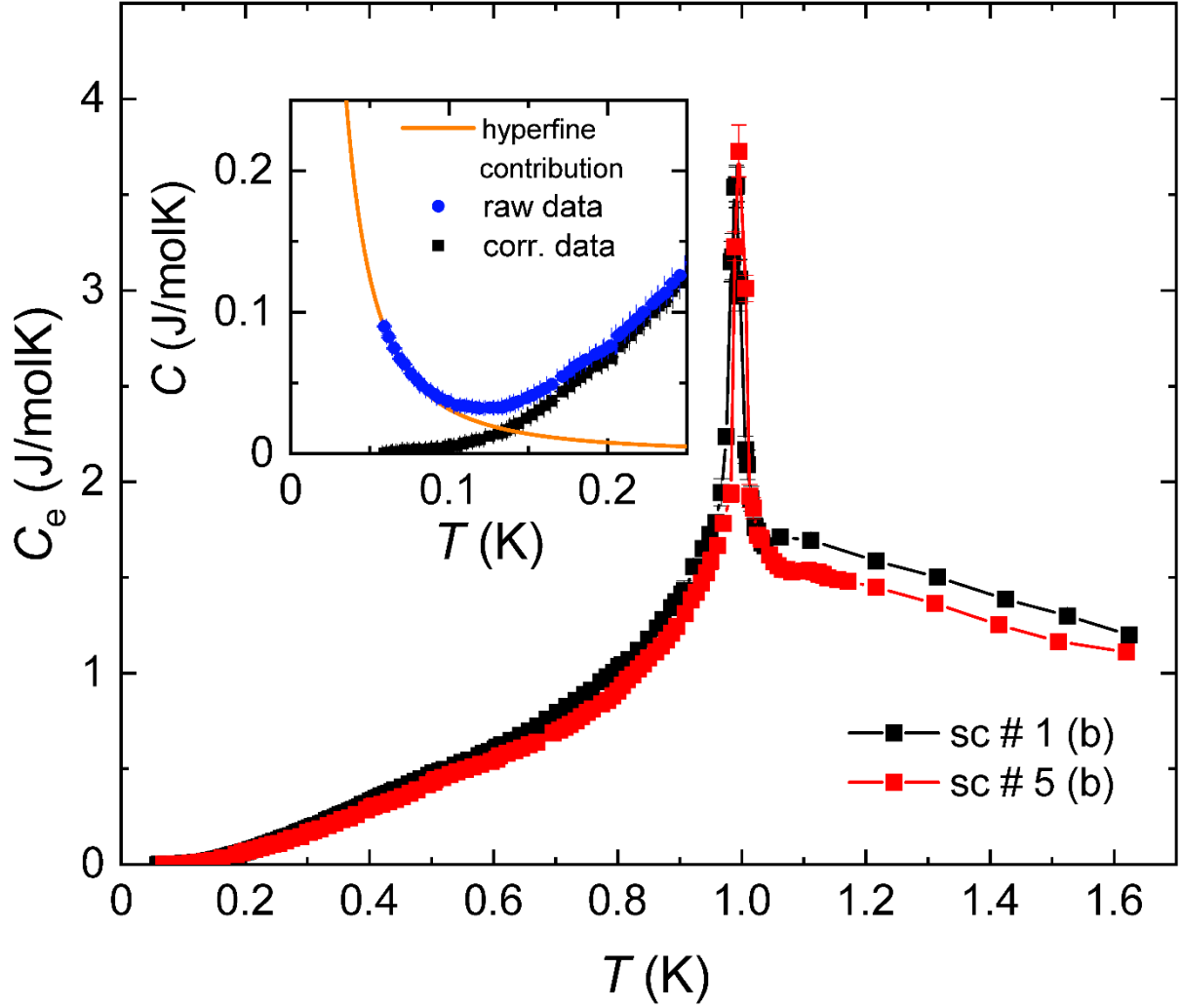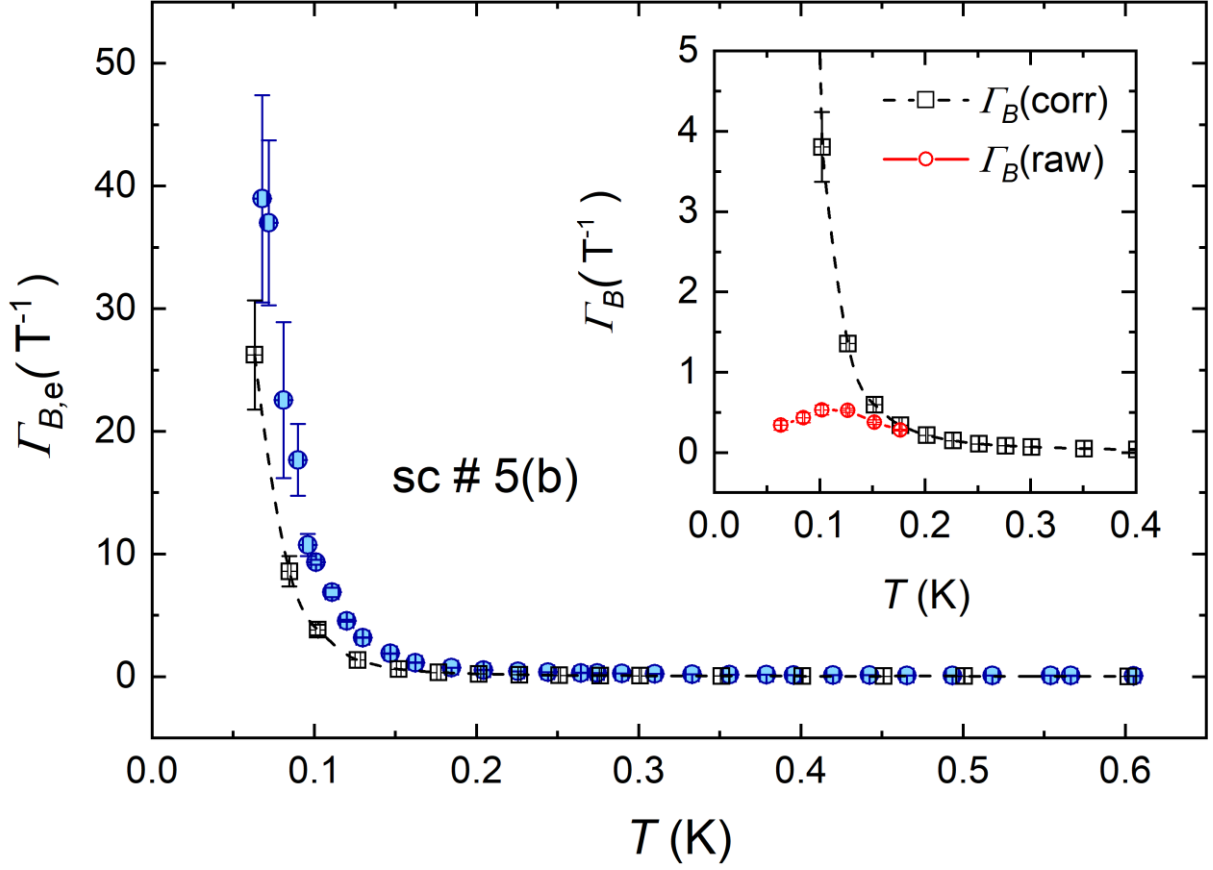
Figure 2. Electronic contribution to the specific heat, C_e, related to the Cu^{2+} electron spins of $PbCuTe_2O_6$ for single crystals #1(b) and #5(b). The inset shows the total specific heat, C, of crystal #1(b) (blue circles) together with the asymptotical low-temperature fit to these data representing the nuclear contribution, C_n, associated with the copper isotopes ^{65}Cu and ^{63}Cu (orange line). As in the main graph the black squares denote the specific heat C_e of the Cu^{2+} electron spins after subtracting the nuclear contribution C_n.

The magnetic Grüneisen parameter of interest $\Gamma_{B,e} = -C_e^{-1}(\partial S_e/\partial B)_T$, which probes the variation of electronic entropy, S_e, with respect to changes of the magnetic field under isothermal conditions, was measured in two different ways.
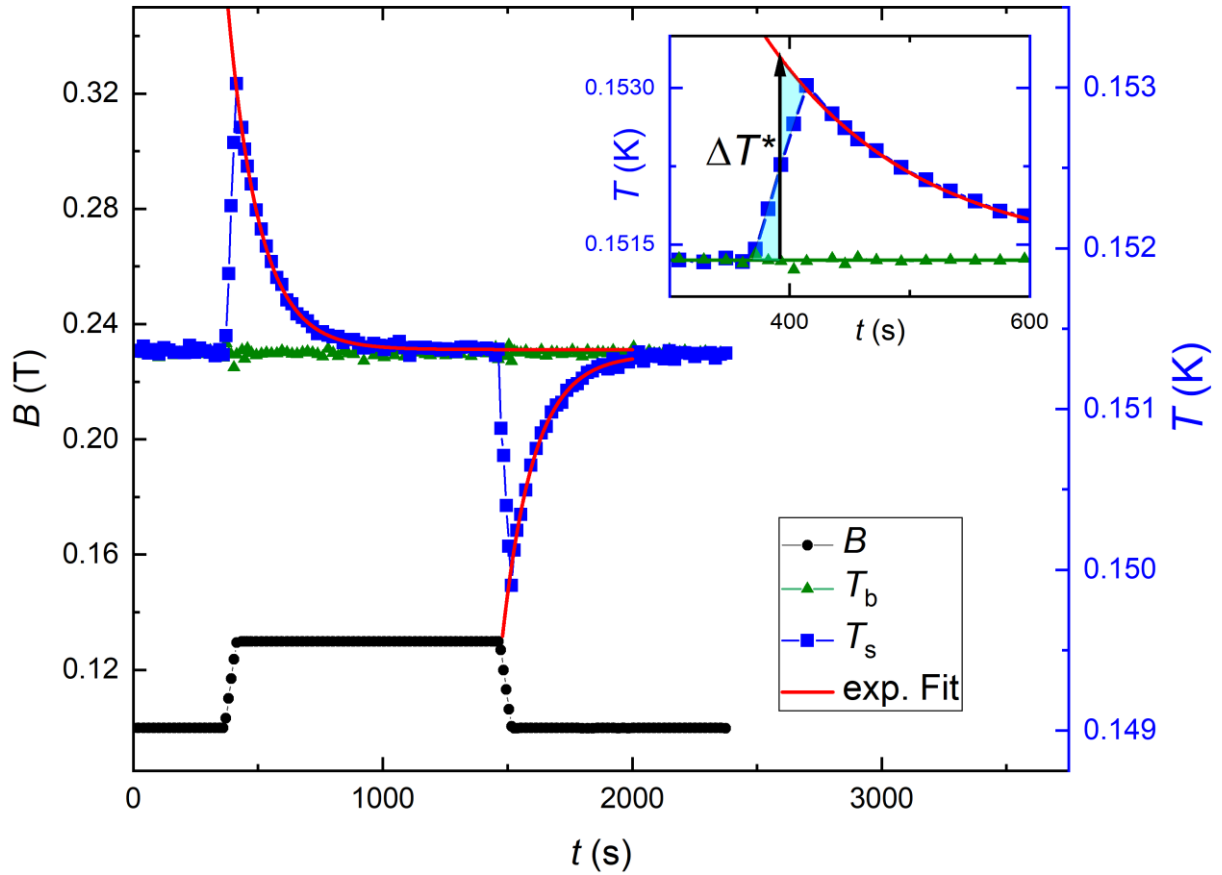
Figure 3. Illustration of a typical measuring cycle for determining the magnetic Grüneisen parameter. At the beginning of the cycle at time $t = 0$, the sample at the temperature T_s is in thermal equilibrium with the bath temperature at $T_s = T_b \approx 0.151$ K. In the example shown, the sample is in a dc field of $B = 0.1$ T. At $t = 400$ s the field is ramped up by $\Delta B = +0.03$ T which is accompanied by an increase in T_s. After the field change is completed, T_s relaxes back to T_b. This relaxation is fitted by an exponential decay $T_s(t) \propto \exp(-t/\tau)$ with τ the relaxation time (red solid line in Fig. 3). By extrapolating the exponential decay back to times at which the field change started, the increase in temperature ΔT^* can be determined from an equal-areas construction as indicated in the inset of Fig. 3.

Figure 4. Temperature dependence of the electronic contribution $\Gamma_{B,e}$ to the magnetic Grüneisen parameter of single crystalline $PbCuTe_2O_6$. The main panel shows $\Gamma_{B,e}$ for sc #5(b), associated with the Cu^{2+} spins, obtained by applying technique (1) described in the text (black open squares) and taking into account the nuclear contributions according to eq. (10). For comparison the figure also shows $\Gamma_{B,e}$ for sc #5(b) obtained by using technique (2) (blue spheres). The inset shows the raw data (red spheres), corresponding to Γ_B, and $\Gamma_{B,e}$ (black open squares) from the main panel for $T \leq 0.4$ K.

The magnetic Grüneisen parameter was also measured as a function of magnetic field at a constant temperature $T = 0.15$ K by using technique (1) described above. The results are shown in Fig. 5 as $1/\Gamma_{B,e}$ vs B. We find a rapid suppression following a $\Gamma_{B,e} \propto (B - B_c)^{-1}$ dependence with $B_c \approx 0$.
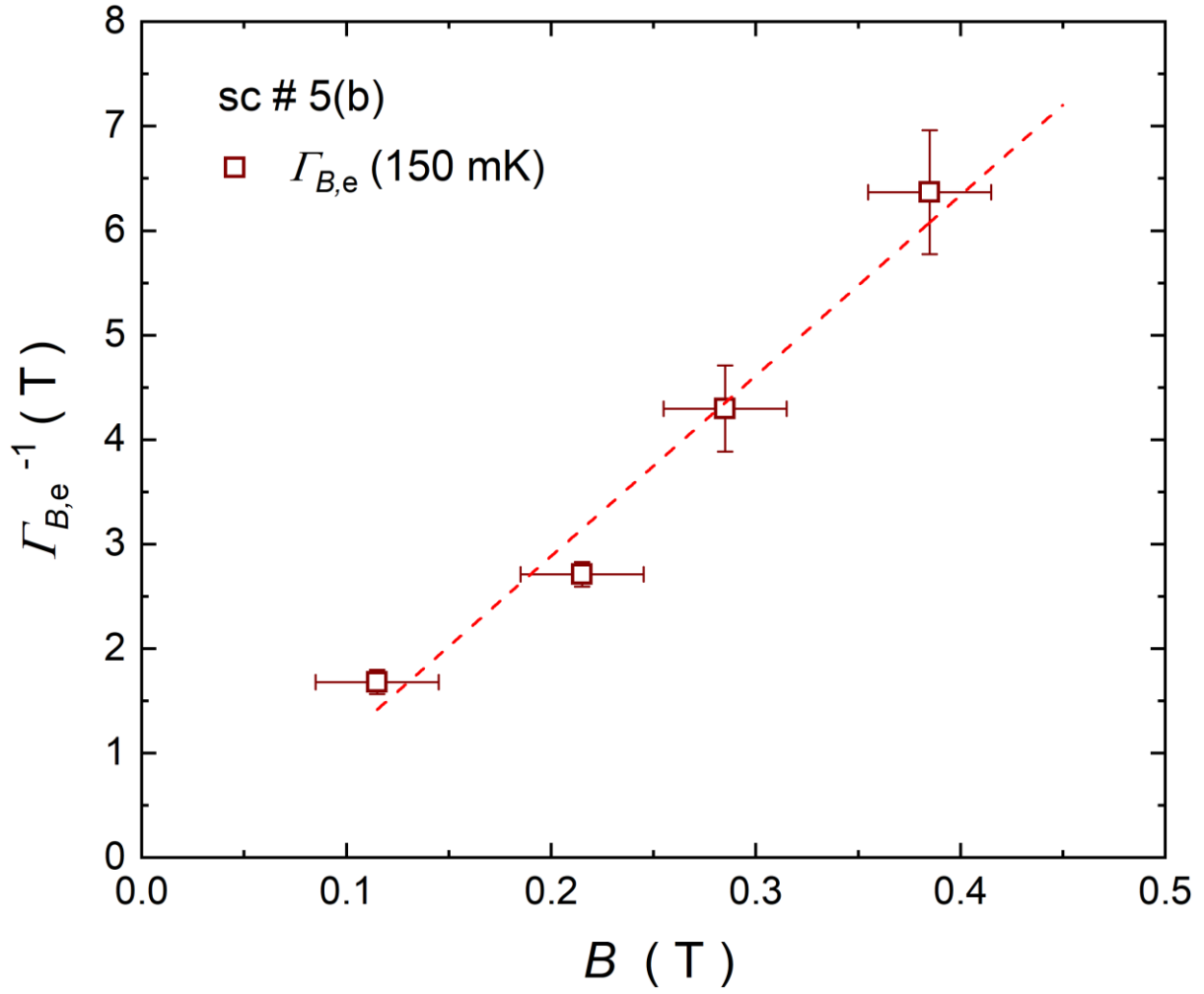
Figure 5. Electronic contribution to the magnetic Grüneisen parameter at a temperature $T = 0.15$ K plotted as $1/\Gamma_{B,e}$ vs. B. The suppression of $\Gamma_{B,e}$ with field approximately follows a behaviour $\Gamma_{B,e} = -A/(B - B_c)$ with $A = 0.058 \pm 0.005$ and $B_c = (0.033 \pm 0.06)$ $T \approx 0$ (broken line).
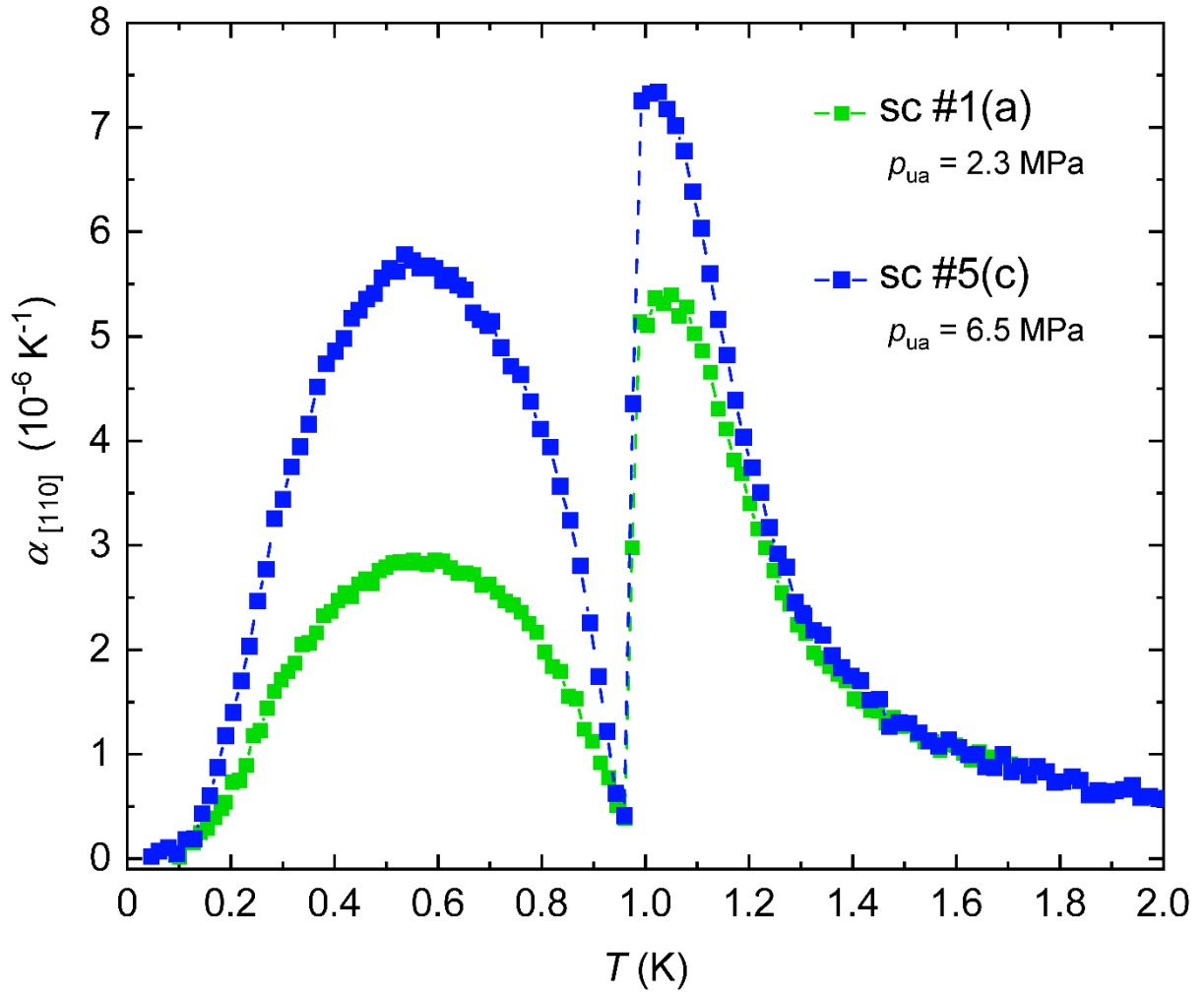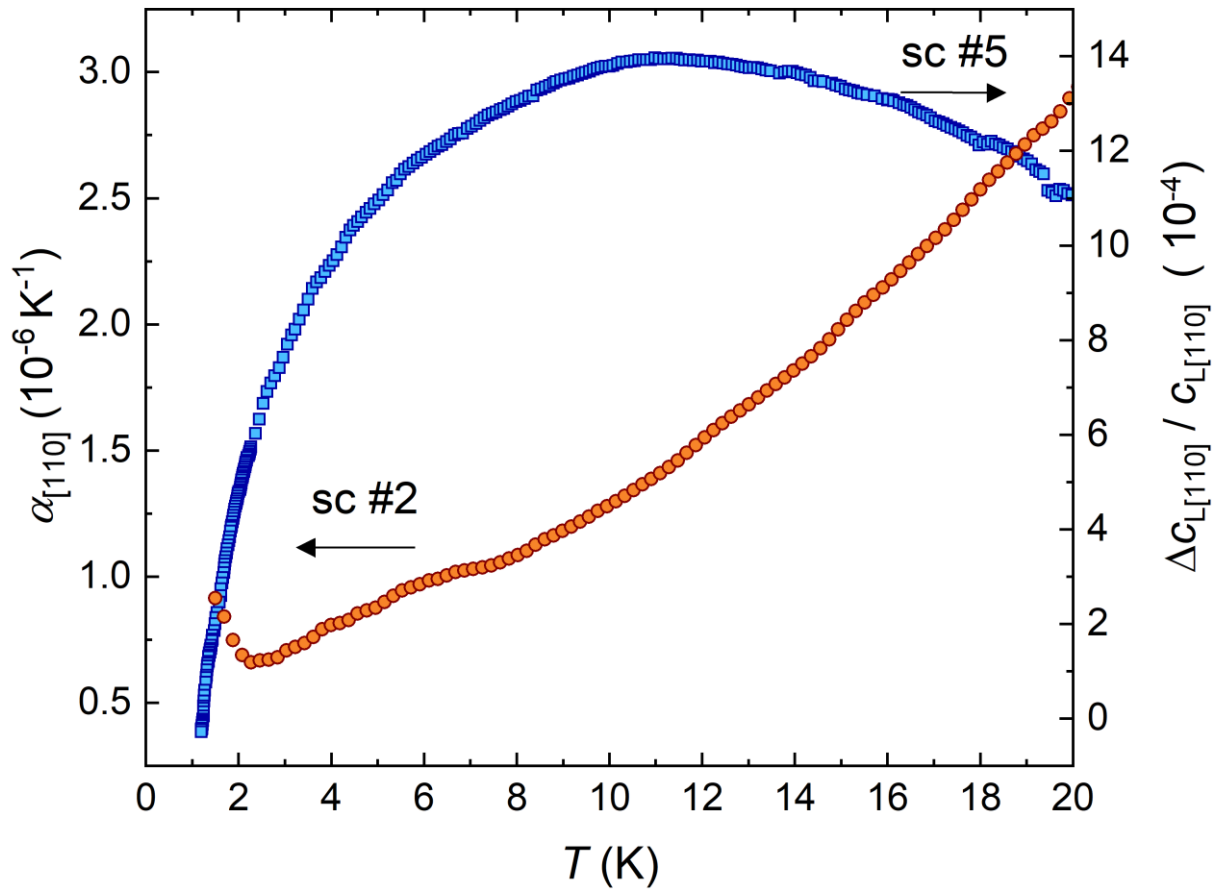
Figure 6. Coefficient of thermal expansion of $PbCuTe_2O_6$ single crystals sc #1(a) measured along the [1-10] direction and sc #5(c) measured along the [110] direction. In these measurements the uniaxial pressure along the measuring direction was p_{ua} = (2.3 ± 0.5) MPa for sc #1(a) and $p_{ua} = (6.5 \pm 1.3)$ MPa for sc #5(c). The pressure values refer to the pressure at around 4 K.
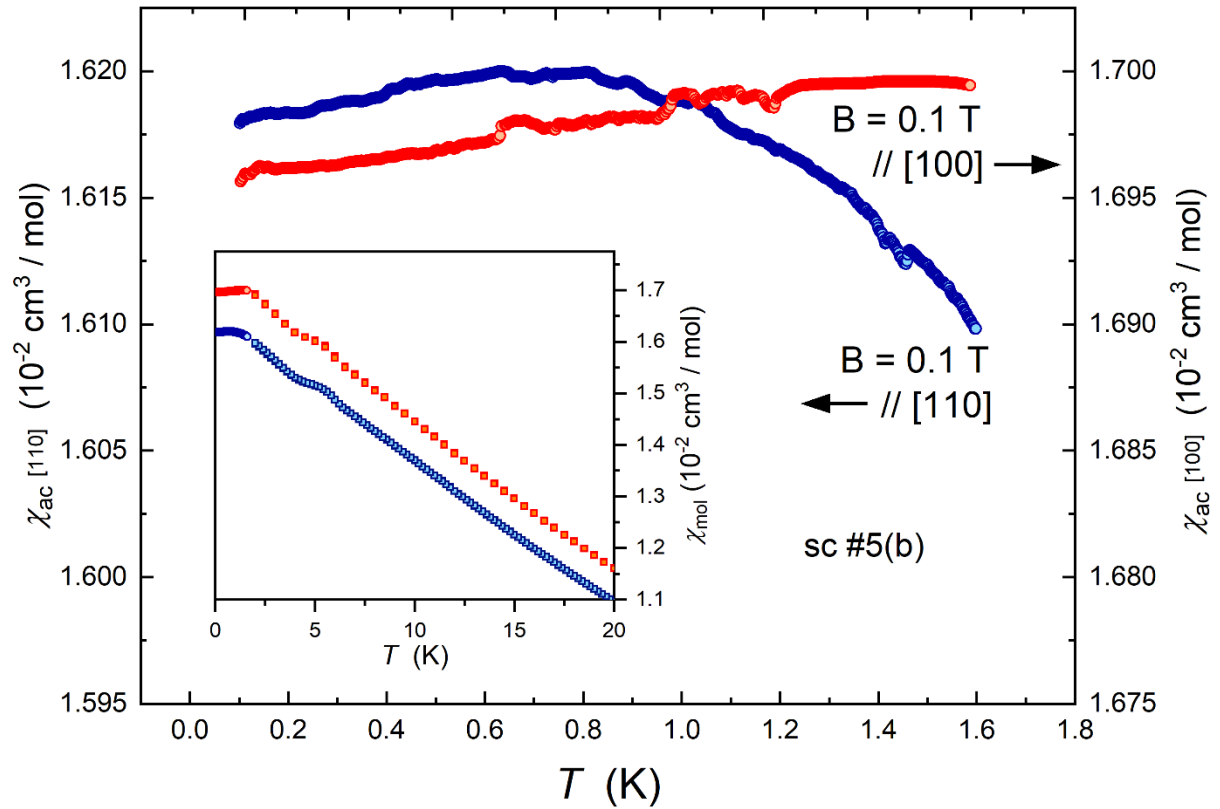
Figure 7. Temperature dependence of the ac-susceptibility, χ_{ac}, of $PbCuTe_2O_6$ single crystal #5(b) for temperatures $0.1\ K \leq T \leq 1.6\ K$. The data were taken in a field of $B = 0.1\ T$ applied along the [100] (red spheres, right scale) and [110] (blue spheres, left scale) directions. The inset shows the same data together with data (same colour code) for $T \geq 2\ K$ measured by using a commercial SQUID magnetometer (Quantum Design).

Figure 8. Coefficient of thermal expansion $\alpha_{[110]}$ for sc #2 together with the longitudinal elastic constant $c_{L[110]}$ for sc #5(a) for temperatures 1.3 K $\leq T \leq$ 20 K.
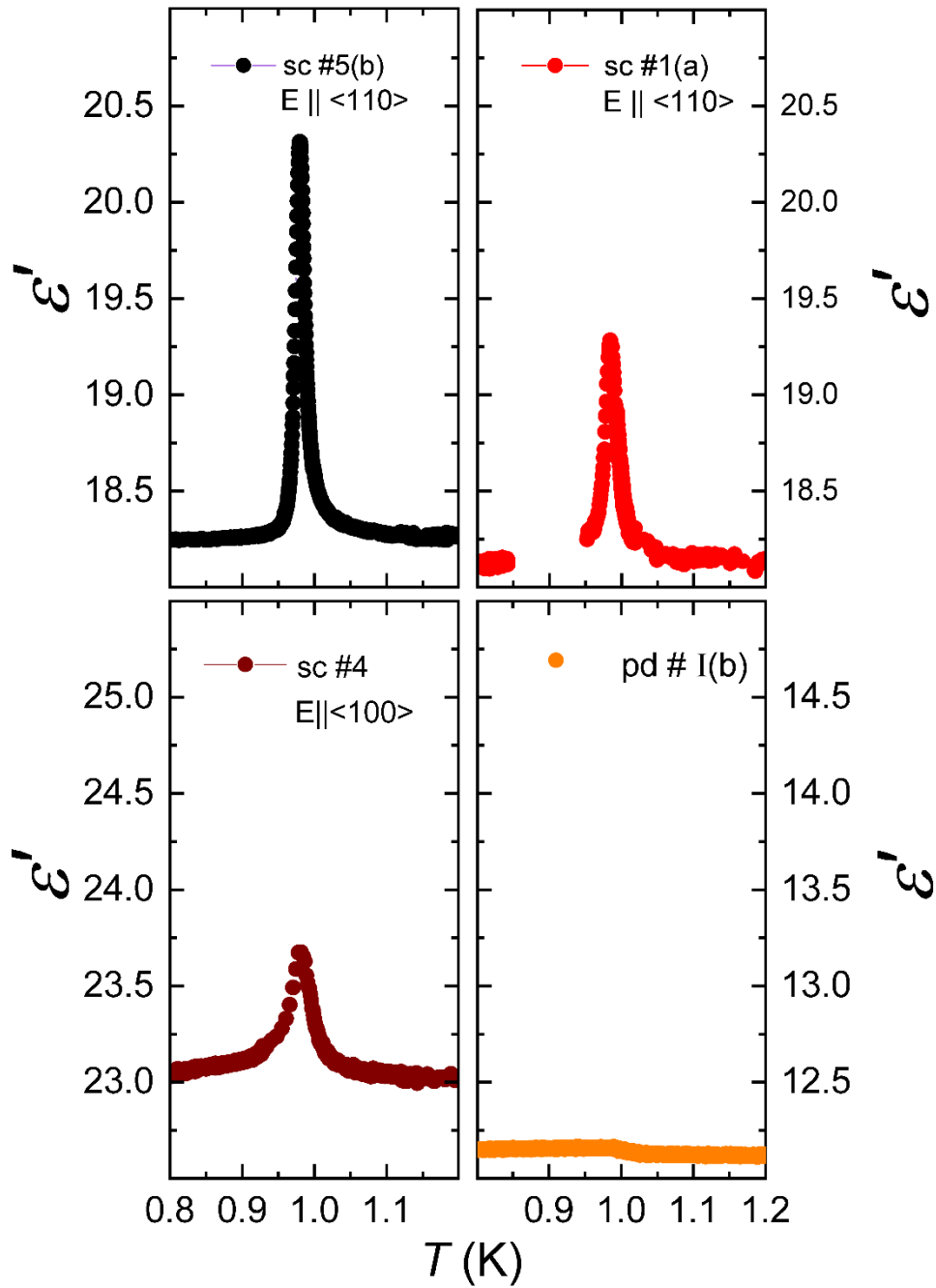
Figure 9. Results of the dielectric constant ε' of PbCuTe$_2$O$_6$ for single crystals sc #5(b) (black spheres, upper left), sc #1(a) (light red spheres, upper right), sc #4 (dark red spheres, lower left), and a pressed-powder sample pd #I(b) (orange spheres, lower right). The orientation of the electric field **E** is indicated in the figure. Data were taken at a frequency of 11 kHz.
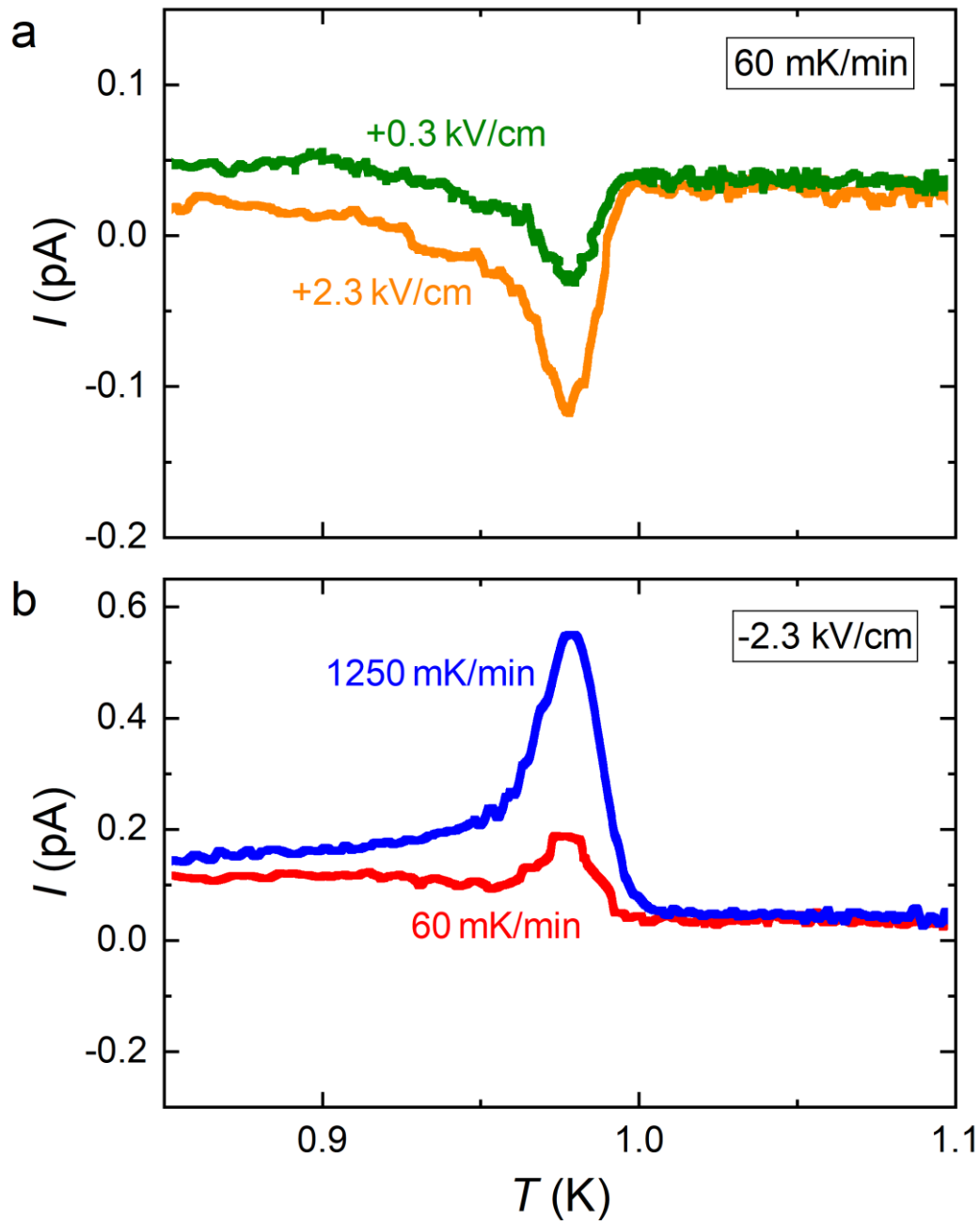
Figure 10. a: Pyrocurrent as measured with identical heating rates for two different poling fields. b: Pyrocurrent measured with two different heating rates for identical poling field.

Supplementary Tables

Isotope	z	I	μ (μ_N)
^{63}Cu	0.692	3/2	2.22
^{65}Cu	0.308	3/2	2.38
^{125}Te	0.143	1/2	0.887
^{207}Pb	0.221	1/2	0.578

$$\mu_N = 5.05095 \cdot 10^{-27} \ J \ T^{-1}$$

Table 1. List of isotopes with their natural abundances z, their nuclear spins I and the associated nuclear magnetic moment μ in units of the nuclear magneton μ_N taken from [4,5].

Supplementary References

[1]   Chillal, S. *et al.* Evidence for a three-dimensional quantum spin liquid in PbCuTe$_2$O$_6$. *Nat. Commun.* **11**, 2348 (2020).

[2]   Weil, M., Shirkhanlou, M., Stürzer, T. Phase formation studies of lead(II) copper(II) oxotellurates: the crystal structures of dimorphic PbCuTeO$_5$, PbCuTe$_2$O$_6$, and [Pb$_2$Cu$_2$(Te$_4$O$_{11}$)](NO$_3$)$_2$. *Zeitschr. f. anorg. und allg. Chemie* **645**, 347-353 (2019).

[3]   Koteswararao, B. *et al.* Magnetic properties and heat capacity of the three-dimensional frustrated S = 1/2 antiferromagnet PbCuTe$_2$O$_6$. *Phys. Rev. B* **90**, 035141 (2014).

[4]   Fuller, G. H. Nuclear spins and moments. *J. Phys. Chem. Ref. Data* **5**, 835-1092 (1976).

[5]   De Bièvre, P. and Taylor, P. D. P. Table of the isotopic compositions of the elements. *Int. J. Mass Spectrom. Ion Processes* **123**, 149-166 (1993).

[6]   Wolf, B. *et al.* Magnetocaloric effect and magnetic cooling near a field-induced quantum-critical point. *Proc. Natl. Acad. Sci. USA* **108**, 6862-6866 (2011).

[7]   Pott, R., Schefzyk, R., Apparatus for measuring the thermal expansion of solids between 1.5 and 380 K., *J. Phys. E* 16, 444-449 (1983).

[8]   Petrashen, V. E., Yablokov, Yu. V., and Davidovich, R. L. The lattice structure parameters and configuration of Cu^{2+} Jahn-Teller centres in Tutton salt crystals. *Phys. Stat. Sol. B* **101**, 117-125 (1980).

[9]   Nakatsuji, S. *et al.* Spin disorder on a triangular lattice. *Science* **309**, 1697-1700 (2005).

[10]   Zhong, W. L. *et al.* Phase transition in $PbTiO_3$ ultrafine particles of different sizes. *J. Phys.: Condens. Matter* **5**, 2619-2624 (1993).

[11]   Chattopadhyay, S., Ayyub, P., Palkar, V. R., Multani, M. Size-induced diffuse phase transition in the nanocrystalline ferroelectric $PbTiO_3$. *Phys. Rev. B* **52**, 13177-13183 (1995).

[12]   Zhao, Z. *et al.* Grain-size effects on the ferroelectric behavior of dense nanocrystalline BaTiO$_3$ ceramics. *Phys. Rev. B* **70**, 024107 (2004).

[13]   Kohara, Y., Yamasaki, Y., Onose, Y., Tokura, Y. Excess-electron induced polarization and magnetoelectric effect in yttrium iron garnet *Phys. Rev. B* **82**, 104419 (2010).

[14]   Nhalil, H. *et al.* Ferromagnetism and the effect of free charge carriers on electric polarization in the double perovskite Y$_2$NiMnO$_6$ *Phys. Rev. B* **92**, 214426 (2015).

[15]   Walsh, A., Payne, D. J., Egdell, R. G., Watson, G. W.   Stereochemistry of post-transition metal oxides: revision of the classical lone pair model *Chem. Soc. Rev.* **40**, 4455-4463 (2011).